Oscillator-Based Inverter Control for Islanded Three-Phase Microgrids

Brian B. Johnson, *Member, IEEE*, Sairaj V. Dhople, *Member, IEEE*, James L. Cale, *Member, IEEE*, Abdullah O. Hamadeh, and Philip T. Krein, *Fellow, IEEE*

Abstract—A control scheme is proposed for an islanded low-inertia three-phase inverter-based microgrid with a high penetration of photovoltaic (PV) generation resources. The output of each inverter is programmed to emulate the dynamics of a nonlinear oscillator. The virtual oscillators within each controller are implicitly coupled through the physical electrical network. The asymptotic synchronization of the oscillators can be guaranteed by design, and as a result, a stable power system emerges innately with no communication between the inverters. Time-domain switching-level simulation results for a 45-kW microgrid with 33% PV penetration demonstrate the merits of the proposed technique; in particular they show that the load voltage can be maintained between prescribed bounds in spite of variations in incident irradiance and step changes in the load.

Index Terms—Microgrids, oscillators, photovoltaic inverter control, synchronization.

I. INTRODUCTION

MICROGRIDS offer the potential for increased renewable generation, improved reliability, and reduced transmission losses. This study is focused on low-inertia islanded microgrids, where sustainable generation resources, such as photovoltaic (PV) arrays and fuel cells (in contrast with diesel-engine or natural-gas-driven generators), are interfaced to the electric network through voltage-source inverters (VSIs), and intermittency in supply is managed by energy storage devices.

Key control challenges in such microgrids include 1) maximizing system availability in the face of uncertain renewable generation, 2) eliminating centralized controllers to ensure there are no single points of failure, and 3) minimizing communication between inverters to enhance resilience against cyber-level failures/attacks. Focused on these challenges, we propose an inverter control paradigm that is inspired by the *synchronization of coupled oscillators*. In particular, a stable islanded microgrid is realized by controlling the VSIs to emulate the dynamics of nonlinear oscillators. When coupled through the underlying electrical network, the virtual oscillators (we use the terminology *virtual* to emphasize that the oscillator dynamics are emulated on a digital controller) synchronize without any supervisory control effort or information exchanges over a communication network; in other words, a stable power system emerges innately by design.

Passivity- and $\mathcal{L}_2$ input-output stability-based methods [1] have recently been proposed in [2]–[4], respectively, to explore the synchronization of coupled nonlinear oscillators with the goal of formulating control strategies for inverters in islanded power systems. In this study, we extend our previous effort in [3] and [4], which was tailored to single-phase inverters, to the control of three-phase inverter-based microgrids with high PV penetration. Toward this end, we also formulate a maximum power point tracking (MPPT) method compatible with the virtual-oscillator-based controller for the subset of PV-interfaced inverters in the microgrid.

Relevant to this study is a wide body of literature on droop control of inverters in islanded microgrids [5]–[11]. Inspired by the control of synchronous generators, this approach is based on modulating the frequency and output voltage of inverters to be inversely proportional to the real and reactive power, respectively [5], [6], [12]–[14]. While the original formulation [5] did not necessitate communication, several drawbacks relating to load sharing accuracy and frequency/voltage deviations have prompted the supplementation of higher level controls, which require a communication network [15]–[19].

The proposed approach that is based on the dynamics of coupled oscillators offers a fundamentally different method for islanded inverter-based microgrids. The intrinsic electrical coupling between inverters is leveraged to synchronize virtual oscillators, hence realizing a control strategy that promotes dynamic load sharing with minimal frequency/voltage deviations. Since each controller is fundamentally identical, the system tolerates failures in any number of inverters so long as the load can be satisfied. The main contributions of this paper are as follows: 1) a method for the synthesis of oscillator-based controllers for three-phase inverters is outlined and 2) an MPPT method is integrated with the oscillator-based controller to maximize the power delivered by PV-interfaced inverters.

Fig. 1.   Schematic of a single dead-zone oscillator.

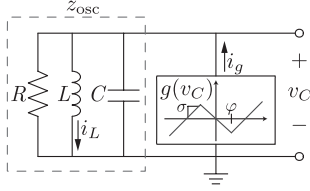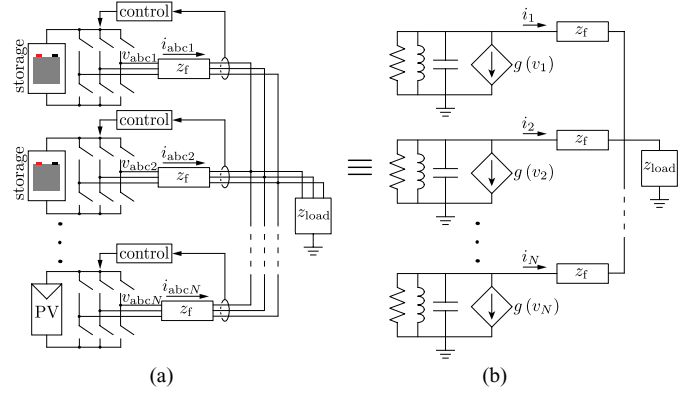Fig. 2.   Microgrid composed of parallel three-phase VSIs in (a) is controlled to emulate the corresponding single-phase system of coupled oscillators in (b).

The remainder of this paper is organized as follows. In Section II, the nonlinear oscillator is introduced, and a method for parameter selection and system design is outlined. Controller implementation details for a three-phase inverter and the MPPT method are described in Section III. Case-studies are presented in Section IV, and these are followed by concluding remarks in Section V.

II. OSCILLATOR MODEL FUNDAMENTALS

In this section, we first present the oscillator model that constitutes the mainstay of the proposed three-phase inverter control method. Then, we provide a sufficient condition that ensures the synchronization of a system of three-phase inverters controlled with the proposed oscillator-based approach. Finally, we describe the parameter selection and system design process.

A. Oscillator Model

Fig. 1 illustrates the nonlinear *dead-zone oscillator* utilized in this study. Each oscillator consists of a resonant LC tank that sets the system frequency, a nonlinear voltage-dependent current source that sustains the oscillations $g(\cdot)$, and a damping element R. The terminal-voltage amplitude is proportional to $(\sigma - 1/R)$, where $\sigma = |\mathrm{d}g/\mathrm{d}v|$, and to ensure oscillations, we must have $\sigma > 1/R$ [3].[1] It can be shown that as $\epsilon := \sqrt{L/C}(\sigma - 1/R) \to 0$, the oscillator terminal voltage is approximately sinusoidal, with frequency $\omega \approx 1/\sqrt{LC}$. This is typically referred to as the quasi-harmonic regime [20].

B. Sufficient Condition for Synchronization

The basic microgrid topology under consideration is composed of parallel VSIs connected to an impedance load as shown in Fig. 2(a). Assume that a subset of the (N total) inverters in the microgrid are interfaced to PV arrays, while the others are interfaced to fuel cells/energy-storage devices (modeled as dc-voltage sources). Each inverter is controlled to emulate the dynamics of the dead-zone oscillator by using the digital controller depicted in Fig. 3 (controller details are outlined subsequently in Section III). With the implementation of the proposed controller, the dynamics of the three-phase microgrid in Fig. 2(a) can be described by the equivalent single-phase system in Fig. 2(b).
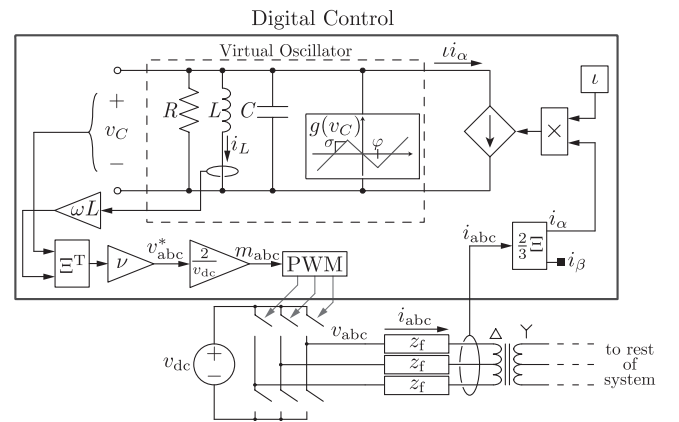

Fig. 3.   Implementation of the proposed controller.

The synchronization of the terminal voltages in the system of coupled oscillators depicted in Fig. 2(b) can be guaranteed if

$$\max_{\omega} \left\| \frac{(\nu\iota)^{-1} z_{\mathrm{f}} z_{\mathrm{osc}}}{(\nu\iota)^{-1} z_{\mathrm{f}} + z_{\mathrm{osc}}} \right\|_2 \sigma < 1 \tag{1}$$

where $\|\cdot\|_2$ denotes the Euclidean norm [1], $z_{\mathrm{f}} = R_{\mathrm{f}} + \mathrm{j}\omega L_{\mathrm{f}}$ is the inverter output-filter impedance, and $z_{\mathrm{osc}} = R \,\|\, \mathrm{j}\omega L \,\|\, (\mathrm{j}\omega C)^{-1}$ is the impedance of the passive RLC circuit in each oscillator (see Fig. 1). Furthermore, the condition in (1) depends on two design parameters, ν and ι (see Fig. 3), that are referred as the voltage and current gains, respectively. The values these parameters are tuned to depend on the voltage and power ratings. Note that for this particular network, the synchronization condition does not depend on the number of inverters N, or the load impedance z_{load}. Assuming a balanced three-phase system, synchronization in the single-phase equivalent system translates to a stable three-phase microgrid. An outline of the proof for the synchronization condition in (1) is provided in Appendix A. Details are in [3].

C. Parameter Selection and System Design

With reference to the controller that is depicted in Fig. 3, the design objective is to select the current gain ι, the voltage gain ν, and the oscillator parameters R, L, C, φ, and σ, for a

---

[1]The terminology *dead-zone oscillator* follows from the fact that we can write $g(v) = f(v) - \sigma v$, where $f(v)$ is a dead-zone function with slope 2σ and $f(v) = 0$ for $v \in (-\varphi, \varphi)$.
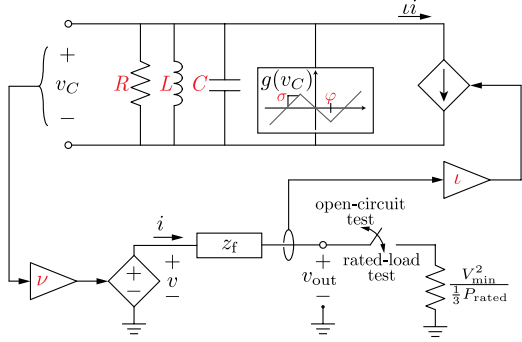
Fig. 4. Circuit model used to perform the open-circuit and rated-load tests for parameter selection. Design parameters that are tuned in Section II-C (R, L, C, σ, φ, ι, and ν) are highlighted in red.
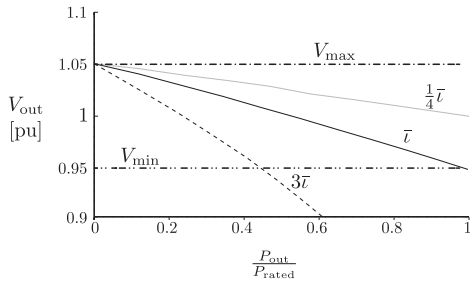

Fig. 5. Inverter output voltage as a function of real power for different values of the current gain. Note that when the current gain is equal to the nominal value, i.e., $\iota = \bar{\iota}$, the output voltage is between $V_{\min} = 0.95$ pu and $V_{\max} = 1.05$ pu for the whole load range.

given filter impedance z_{f}, such that the load voltage and system frequency meet performance specifications. Additionally, the choice of parameters must ensure that the condition in (1) is satisfied. Once all parameters are selected, it is straightforward to discretize the differential equations of the oscillator circuit in Fig. 3 for implementation on a microcontroller.

First, we set $\nu = \sqrt{2}V_{\mathrm{rated}}$, where V_{rated} is the rated RMS line-neutral voltage. This ensures that the virtual oscillator voltage corresponds to the per-unitized inverter voltage. To ensure oscillations at the rated system frequency ω_{rated}, the values of R, L, and C must be selected such that $R > 1/\sigma$, and $LC = 1/\omega_{\mathrm{rated}}^2$. Next, we perform two tests to tune φ and ι such that the RMS load voltage is between prescribed minimum and maximum values, denoted as $V_{\min}$ and $V_{\max}$, respectively. These tests are run for the equivalent single-phase test circuit shown in Fig. 4. In the open-circuit test, the value of φ is tuned so that the RMS voltage at the inverter output V_{out}, equals $V_{\max}$. In the rated-load test, the maximum rated load is connected to the inverter, and ι is adjusted such that $V_{\mathrm{out}} = V_{\min}$. The value of ι computed after the rated-load test is referred to as the nominal current gain, and denoted by $\bar{\iota}$. Finally, (1) is evaluated to validate that the synchronization condition is satisfied.

Fig. 5 illustrates the voltage versus power characteristic of a single inverter for three different choices of the current gain. The complete list of parameters for this particular inverter design is summarized in Appendix B. Note that for a fixed terminal voltage, the inverter output power is inversely proportional to
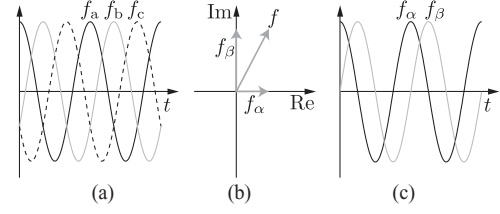

Fig. 6. (a) Illustrative three-phase balanced waveforms (b) Space-vector signal in the complex plane. (c) Corresponding waveforms in the $\alpha\beta$-frame.

ι. This characteristic forms the basis of the MPPT method (see Section IV-B) for the PV-interfaced inverters.

III. OSCILLATOR-BASED INVERTER CONTROL METHOD

In this section, we outline key controller implementation details that ensure the three-phase inverters emulate the behavior of the dead-zone oscillator described in Section II-A (the schematic of the controller is illustrated in Fig. 3). In the forthcoming discussions, we particularly focus on the coordinate transformations that interface the oscillator to the three-phase inverter, and describe the MPPT strategy that has been adopted for the PV-interfaced inverters in the microgrid.

A. Three-Phase Controller Design

Controller design in three-phase inverters can be simplified by formulating suitable coordinate transformations that refer three-phase voltages and currents to a different reference frame [21]. In this study, we focus on controller design in the $\alpha\beta$ frame [21]. Toward this end, for a set of balanced, sinusoidal, three-phase waveforms $f_{\mathrm{a}}(t)$, $f_{\mathrm{b}}(t)$, $f_{\mathrm{c}}(t)$, define the *space vector* signal

$$f(t) := \frac{2}{3}(f_{\mathrm{a}}(t) + f_{\mathrm{b}}(t)\mathrm{e}^{\frac{-2\pi}{3}\mathrm{j}} + f_{\mathrm{c}}(t)\mathrm{e}^{\frac{2\pi}{3}\mathrm{j}}). \quad (2)$$

The real and imaginary components of $f(t)$ are denoted by $f_{\alpha}(t)$ and $f_{\beta}(t)$, respectively. The relationship between the original three-phase signals and the transformed signals in the $\alpha\beta$-frame is captured by the following:

$$\begin{bmatrix} f_{\alpha} \\ f_{\beta} \end{bmatrix} = \frac{2}{3}\Xi \begin{bmatrix} f_{\mathrm{a}} \\ f_{\mathrm{b}} \\ f_{\mathrm{c}} \end{bmatrix}, \quad \begin{bmatrix} f_{\mathrm{a}} \\ f_{\mathrm{b}} \\ f_{\mathrm{c}} \end{bmatrix} = \Xi^{\mathrm{T}} \begin{bmatrix} f_{\alpha} \\ f_{\beta} \end{bmatrix} \quad (3)$$

where

$$\Xi := \begin{bmatrix} 1 & -\dfrac{1}{2} & -\dfrac{1}{2} \\[2mm] 0 & \dfrac{\sqrt{3}}{2} & -\dfrac{\sqrt{3}}{2} \end{bmatrix}. \quad (4)$$

Fig. 6 depicts the coordinate transformation described previously for an illustrative set of three-phase signals.

As shown in Fig. 3, the aforementioned coordinate transformation is used in the controller in two key ways. First, the inverter output currents, $i_{\mathrm{abc}}(t) = [i_{\mathrm{a}}(t), i_{\mathrm{b}}(t), i_{\mathrm{c}}(t)]^{\mathrm{T}}$, are sensed and transformed to obtain $i_{\alpha}(t)$ and $i_{\beta}(t)$ with (3). Since $i_{\mathrm{a}}(t) = i_{\alpha}(t)$ under balanced conditions, the current $\iota i_{\alpha}(t)$ is extracted from the virtual oscillator to establish the link with the single-phase equivalent of the three-phase inverter. Next,
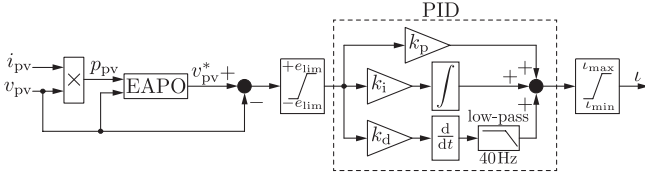
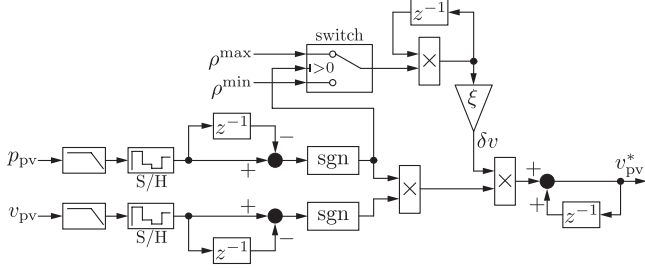Fig. 7. Block diagram of MPPT controller for PV-interfaced inverters.

Fig. 8. Details of the exponential adaptive perturb and observe MPPT algorithm utilized in this study.

to control the switching action of the three-phase inverter, a set of three-phase modulation signals must be generated. In the quasi-harmonic regime, we can approximate the oscillator terminal voltage as $v_C(t) = V \cos(\omega t)$, where, as described in Section II, the amplitude V, is governed by the choice of σ and R, and the frequency $\omega \approx 1/\sqrt{LC}$. Since $di_L/dt = v_C$, it follows that the current through the inductor in the RLC subcircuit is given by $i_L(t) = V/(\omega L) \sin(\omega t)$. Since $v_C(t)$ and $i_L(t)$ are orthogonal, they can be used to derive a set of three-phase modulation signals. In particular, v_C and i_L are transformed from the $\alpha\beta$-frame to the abc-frame, multiplied by ν, and scaled by the dc-link voltage to yield a set of three-phase modulation signals $m_{abc}(t) = [m_a(t), m_b(t), m_c(t)]^T$. Finally, a conventional sine-triangle pulse width modulation scheme [22] is used to generate the switching signals. With the proposed approach, the inverter terminal voltages follow the commanded voltages, i.e., $v_{abc} \rightarrow v_{abc}^*$.

Remark 1: Note that with the proposed approach, the controller state variables corresponding to the nonlinear oscillator [i.e., $v_C(t)$ and $i_L(t)$] are directly utilized to generate the three-phase modulation signals. This eliminates the need for explicit orthogonal-signal generators [23], [24].

B. Maximum Power Point Tracking Method

We now describe the MPPT controller for the subset of PV-interfaced inverters in the microgrid. The exponential adaptive perturb and observe (EAPO) algorithm is utilized for MPPT [25]. This method is similar in construction to other adaptive perturb and observe (PO) algorithms (see, e.g., [26]–[28]) that modulate the perturbation step size with a goal of improving the dynamic and steady-state performance. In particular, these methods can potentially increase tracking speed and improve tracking efficiency by reducing oscillations around the maximum power point in a periodic steady state.

A block diagram of the MPPT controller is shown in Fig. 7, and the details of the EAPO algorithm are illustrated in Fig. 8.

We utilize the PV voltage as the MPPT perturbation control variable. As demonstrated in [29], this results in a fast response to irradiance changes and presents significant advantages compared with using the PV current as the control variable. Before discussing the details of the EAPO algorithm, it will be useful to briefly summarize the conventional PO algorithm. In a conventional PO algorithm, the dc-bus voltage reference in the $k+1$ iteration, $v_{pv}^*[k+1]$, is updated as follows:

$$v_{pv}^*[k+1] = v_{pv}^*[k] + \delta v \cdot \text{sgn}(\Delta v_{pv}[k])\text{sgn}(\Delta p_{pv}[k]) \quad (5)$$

where δv is the size of the perturbation step, $v_{pv}^*[k]$ is the dc-bus voltage reference, $\text{sgn}(\Delta v_{pv}[k])$ is the sign of the difference in the dc-bus voltage, and $\text{sgn}(\Delta p_{pv}[k])$ is the sign of the difference in the extracted PV power (all for the kth iteration). With a conventional PO algorithm, note that the perturbation step size δv, is fixed; the precise choice is based on a tradeoff in tracking speed and size of periodic steady-state oscillations around the maximum power point. To address these concerns, in the EAPO algorithm, the dc-bus voltage reference is updated as follows:

$$v_{pv}^*[k+1] = v_{pv}^*[k] + \delta v[k+1] \cdot \text{sgn}(\Delta v_{pv}[k])\text{sgn}(\Delta p_{pv}[k]) \quad (6)$$

where the perturbation step size is updated according to

$$\delta v[k+1] = \begin{cases} \rho^{\max}\delta v[k], & \text{if } \Delta p_{pv}[k] > 0 \\ \rho^{\min}\delta v[k], & \text{otherwise.} \end{cases} \quad (7)$$

Essentially, the perturbation step size is increased by a large factor $\rho^{\max}$ (small factor $\rho^{\min}$) if the extracted power increased (decreased) in the previous iteration. As shown in Fig. 8, a scaling factor ξ, can be included if required. In particular, the algorithm formulation ensures that the perturbation step size is reduced close to the maximum power point; this significantly increases the tracking efficiency in a periodic steady state [25].

A PID controller acts on the dc-bus voltage error $v_{pv}^* - v_{pv}$, and modulates the current gain ι. Since the power output of each inverter is inversely proportional to ι (see Fig. 5), this strategy ultimately controls the power output to ensure the dc-bus voltage is regulated to the reference that is generated by the MPPT algorithm. This general approach, where the dc-link voltage is regulated via the inverter power output, is widely adopted in VSIs with dc power-source inputs [21].

It is worth mentioning that while we apply the EAPO method for simplicity and ease of implementation, other approaches could be investigated to generate the dc-bus voltage reference (see [30]–[33] for comparisons and reviews of established MPPT methods, and [34]–[37] for some recent work in this area).

Remark 2: The controller depicted in Fig. 3 is utilized to regulate *all* inverters. The MPPT algorithm essentially constitutes a secondary outer control loop to modulate the current gain *only* in the PV-interfaced inverters. The current gains of the other inverters are fixed to the nominal value $\bar{\iota}$, determined following the design procedure outlined in Section II-C.

IV. CASE STUDIES

In this section, we demonstrate the performance of the proposed oscillator-based controller with three case studies. The
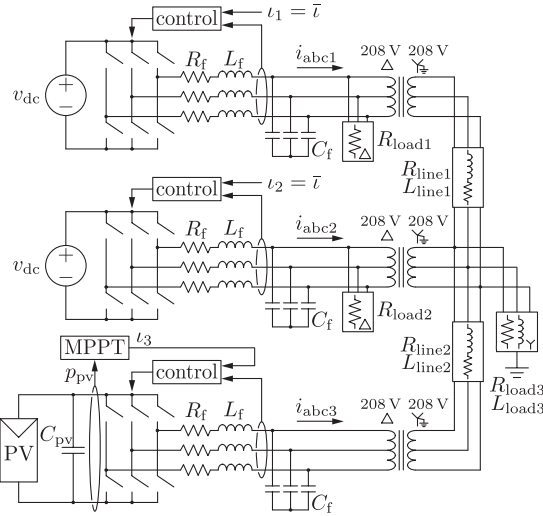
Fig. 9. Islanded microgrid composed of two inverters interfaced to energy-storage devices and one inverter interfaced to a PV array.
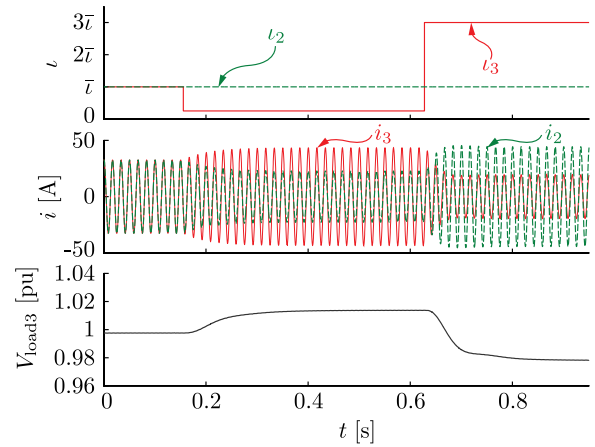

Fig. 10. Dynamics of a two inverter system when ι_2 is fixed and ι_3 undergoes step changes.

Fig. 11. Microgrid synchronization during startup.

simulations are performed for different abstractions (with increasing complexity) of the islanded microgrid system illustrated in Fig. 9. The three-phase inverters are each rated to deliver 15 kW. Two of the inverters (inverters 1 and 2) are connected to energy-storage devices (modeled as dc-voltage sources for the time scales investigated), and one inverter (inverter 3) is interfaced to a PV array, which is modeled using the single-diode model [38]. There are three loads in the system: loads 1 and 2 are resistive, and local to inverters 1 and 2 (R_{load1} and R_{load2} in Fig. 9), while load 3 is an inductive load (R_{load3}, L_{load3} in Fig. 9). Delta-wye transformers facilitate lower dc-link voltages and are not a fundamental requirement of the proposed approach. The rated line-line voltage is 208 V and control parameters are selected to ensure that the common-load voltage is within $\pm 5\%$ of the rated value at 60 Hz under all operating conditions. The virtual-oscillator controller that has been depicted in Fig. 3 is employed in all three inverters. For the PV-interfaced inverter, MPPT is implemented following the approach described in Section IV-B. The parameters of the controller and the PV array are summarized in Appendix B. The perturbation frequency is set to 4 Hz, and this choice is based on the PV dc-link capacitance, which governs the PID voltage regulator settling time. For all cases, controller parameters are picked so that the synchronization condition in (1) is satisfied.

In the first case study, we demonstrate how dynamic load sharing between inverters is promoted by the terminal voltage-power characteristics in Fig. 5. The second and third case studies investigate system performance under variable irradiance and load conditions, respectively.

A. Dynamic Load Sharing

As described in Section II-C, the current gain of each inverter is selected such that the steady-state inverter output voltage is between prescribed lower and upper voltage limits ($V_{\min}$ and $V_{\max}$, respectively) across the entire load range (open-circuit to full rated load). Additionally, for a given terminal voltage,
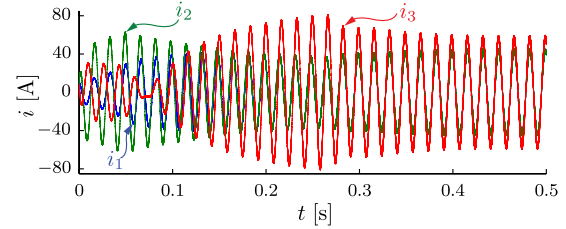
the power output is inversely proportional to the value of ι, as shown in Fig. 5. In this case study, we demonstrate that when a subset of inverters is allowed to vary the current gain (as would be the case with the MPPT controller in Fig. 7), the proportion of power delivered by each inverter also varies.

Consider the microgrid in Fig. 9, except, only with inverters 2 and 3. For simplicity, neglect the line impedances and the local loads, and assume a common resistive load. Since the primary aim of this case study is to illustrate the impact of variable current gains on load sharing, the inputs to the inverters are fixed to be dc-voltage sources. Furthermore, the current gain of inverter 2 ι_2, is fixed, while that of inverter 3 ι_3, is varied manually. Fig. 10 shows the system dynamics as ι_3 undergoes a series of step changes. The inverters share the load equally when $\iota_2 = \iota_3$. However, as ι_3 rises above and falls below ι_2, its fraction of load current (power) decreases and increases, respectively. In light of the terminal characteristics in Fig. 5, the load voltage is always constrained to lie between $V_{\min}$ and $V_{\max}$ as ι_3 varies. In subsequent simulation studies, we will find that consequently, the common-load voltage satisfies performance objectives in spite of variations in ambient conditions and load power.

B. Synchronization and MPPT Operation

At startup, the virtual-oscillator capacitor voltages were initialized to $v_C(0) = [0.25, 0.28, 0.22\,\mathrm{V}]^{\mathrm{T}}$. Fig. 11 illustrates the phase-a currents of the three inverters during this startup. In spite of mismatched initial conditions, the inverters successfully reach the desired synchronized steady-state condition with
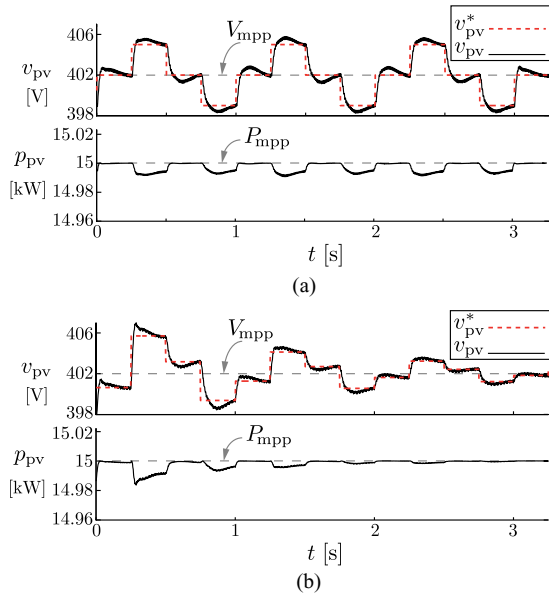
Fig. 12. Dynamics of the PV dc bus approaching the steady state as MPPT algorithms are initiated, comparing (a) the conventional PO algorithm of (5) to (b) the EAPO algorithm of (6). The maximum power point voltage and power are given by $V_{\mathrm{mpp}} = 402\,\mathrm{V}$ and $P_{\mathrm{mpp}} = 15\,\mathrm{kW}$, respectively. The system control parameters support a perturbation frequency of 4Hz, and the PV dc bus recovers within about 0.2 s from each algorithm step. Note that the adaptive step size of the EAPO algorithm gets closer to the maximum power point and provides better tracking efficiency than conventional PO within 1 s after the MPPT algorithms begin to act.
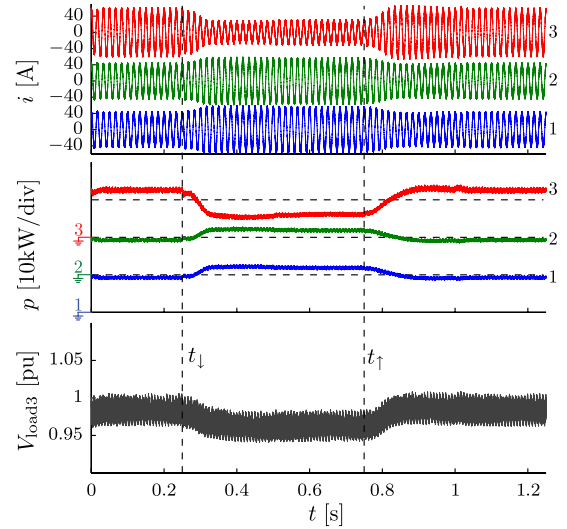

Fig. 13. Inverter (phase-a) currents, power outputs, and load voltage in the microgrid network with a resistive common load and no local loads. The PV irradiance decreases and increases abruptly at $t_{\downarrow}$ and $t_{\uparrow}$, respectively.

all currents in phase. The start-up process limits current flows. Inverter 3 shows the highest overshoot, less than 35% of the final steady-state condition, and the overshoot lasts only about five cycles. Convergence is achieved for the three-inverter system from this blackstart condition in less than 20 cycles. Inverters 1 and 2 are in phase within about three cycles, and inverter 3 pulls into phase in the transition between cycles five and six—changing by more than 90° in one cycle but without imposing substantial current. Thus, the synchronization process takes only about 0.1 s and convergence to target power flows takes a bit longer, at about 0.3 s. The steady-state power injected by the PV inverter (unit 3) is 15 kW and corresponds to the maximum power point. Fig. 12 compares the dynamic recovery of the PV dc-bus voltage as the system approaches the steady state. The upper traces in Fig. 12(a) show a conventional PO process with about 1% voltage resolution. It oscillates around the maximum power point ($V_{\mathrm{mpp}} = 402\,\mathrm{V}$ and $P_{\mathrm{mpp}} = 15\,\mathrm{kW}$), imposing a continuing small power error. The traces confirm that this system will support perturbation step rates of at least four steps per second, only a little more aggressive than the 0.3 s large-signal convergence time of the synchronizing control. When the PO algorithm imposes a voltage step, the system recovers within about 0.2 s (essentially a small perturbation effect related to Fig. 11) to allow the assessment of the new power level and provide information for a decision about the next step. In contrast, the EAPO algorithm results represented in the lower traces (see Fig. 12(b)) show that step size can reduce adaptively and quickly. The EAPO algorithm also allows at least four steps per second and recovers within 0.2 s for each step, but in this case,

after four steps it is closer to the the maximum power point than the conventional PO controller, and continues to refine the accuracy to drive power error close to zero. With conventional PO, such a small step size would compromise dynamic response, but the EAPO large-signal dynamics can be designed to be just as fast as conventional PO.

C. Robustness to Irradiance and Load Variations

In this case study, we demonstrate that variations in incident irradiance and load power tend to be absorbed by the energy-storage-interfaced inverters, hence minimizing disruptions in the synchronized operation of the inverters. First, assume that the local loads at inverters 1 and 2 do not consume any power. In addition, the impedances of lines 1 and 2 are set to zero, such that all three inverters are directly connected across the common load. With these assumptions, we recover the network introduced in Section II-B (see Fig. 2), for which satisfying (1) ensures the inverter terminal voltages are synchronized in the steady state. Fig. 13 illustrates system dynamics when a 50% drop in incident illumination is effected at time $t = t_{\downarrow}$. As a result, power delivered by the PV inverter decreases quickly, and must be made up by the other inverters. As the center power traces in Fig. 13 show, the PV inverter tracks the step change within less than 0.1 s. The other inverters pick up quickly enough that the voltage trace at the bottom of Fig. 13 drops by less than 3% during the transient. The ac currents in the top traces mirror the power change, demonstrating that synchronization is maintained even in the face of this fast dynamic imbalance. Subsequently, at time $t = t_{\uparrow}$, the illumination is restored and the inverters recover to the prior condition within 0.1 s. The voltage also recovers. In general, the selected design parameters support extreme dynamic changes, while maintaining the output voltage magnitude inside a $\pm 5\%$ window with no communication between the three inverters.
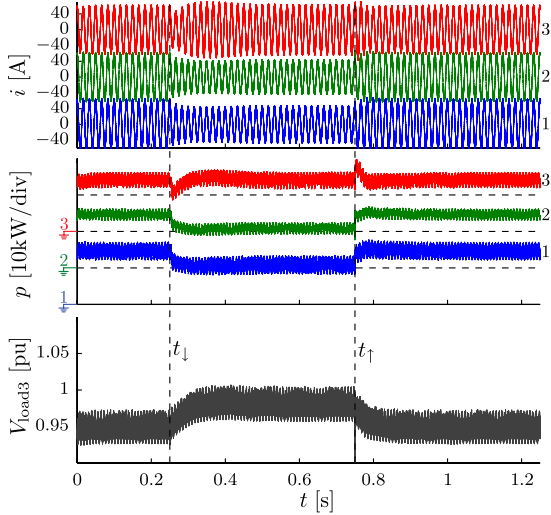
Fig. 14. Inverter (phase-a) currents, power outputs, and load voltage in the microgrid network with local loads and feeder impedances. The common-load power decreases and increases instantaneously at $t_\downarrow$ and $t_\uparrow$, respectively.

Now consider that the local loads at the terminals of inverters 1 and 2 are designed to consume 10 and 5 kW, respectively. As indicated in Appendix B, the common load is inductive, and therefore, the total load power factor is not unity. Additionally, nonzero and nonidentical line impedances connect each inverter to the central load. With this setup, while the inverters are still designed to satisfy (1), the inverter terminal voltages are no longer expected to be synchronized. Nonetheless, we will find that stable operation can be ensured irrespective of load variations. For simplicity, we hold the irradiance constant in this case study. Fig. 14 illustrates the load voltage, and the inverter current and power outputs as the common load undergoes a series of changes. In particular, at time $t = t_\downarrow$, the load is suddenly decreased. Despite the load change, the PV inverter continues to deliver maximum PV power while the other inverters decrease their power output. Next, the load is increased to its original value at time $t = t_\uparrow$ and the power extracted from the energy-storage devices is automatically increased. As before, in all cases the load voltage is maintained within $\pm 5\%$ of the rated value with no communication between the three inverters.

V. CONCLUSION

A technique for controlling a system of inverters in a microgrid has been presented. The proposed method is based on modulating the ac output of each inverter such that it emulates the dynamics of a nonlinear oscillator. Due to the inherent coupling between the oscillators introduced by the electrical network, the inverter ac outputs synchronize. The controllers only require local measurements available at the ac terminals; communication between inverters is not necessary. Oscillator-based control is applied toward the design of a three-phase microgrid with high PV penetration. Simulation results for a 45 kW system demonstrated that the system of inverters continually adjust their output to match load while maximizing PV energy delivery in the face
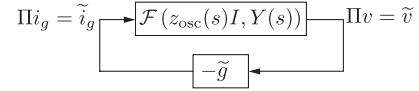

Fig. 15. Block-diagram representation of the differential system. The linear and nonlinear portions of the system are compartmentalized in $\mathcal{F}(\cdot,\cdot)$ and $\widetilde{g}$, respectively.

of uncertainty in ambient conditions and variations in the load power.

APPENDIX A

SKETCH OF THE PROOF FOR THE RESULT IN (1)

The forthcoming discussion is abstracted from [3, Th. 1]. Denote the vector of output currents and terminal voltages of the system of oscillators in Fig. 2(b) by $i = [i_1, \ldots, i_N]^\mathrm{T}$ and $v = [v_1, \ldots, v_N]^\mathrm{T}$, respectively. Additionally, denote the vector of currents sourced by the nonlinear voltage-dependent current sources in the oscillators by $i_\mathrm{g} = [i_{\mathrm{g}1}, \ldots, i_{\mathrm{g}N}]^\mathrm{T}$. Note that $i_\mathrm{g} = -g(v) := [-g(v_1), \ldots, -g(v_N)]^\mathrm{T}$.

We can express $i(s) = Yv(s)$, where Y is the admittance matrix of the microgrid electrical network given by $Y = \alpha I + \beta \Gamma$, where $\alpha = (z_\mathrm{f} + N z_\mathrm{load})^{-1}$, $\beta = z_\mathrm{load}(z_\mathrm{f}(z_\mathrm{f} + N z_\mathrm{load}))^{-1}$, I is the $N \times N$ identity matrix, and Γ denotes the Laplacian of the underlying graph.

To explore voltage synchronization, it is easier to consider the corresponding *differential system*, $\widetilde{i} = \Pi i$, $\widetilde{v} = \Pi v$, and $\widetilde{i}_\mathrm{g} = \Pi i_\mathrm{g}$, with $\Pi = (I - (1/N)\mathbf{1}\mathbf{1}^\mathrm{T})$, where $\mathbf{1} \in \mathbb{R}^N$ denotes the column vector of all ones. The entries of $\widetilde{v}(t)$ track the differences between corresponding entries of $v(t)$ and the average of all entries of $v(t)$ [39]. Consequently, to ensure synchronization, we need to ensure that $\widetilde{v}(t) \to 0$, i.e., the stability of the differential system implies synchronization of the original system.

For ease of analysis, we compartmentalize the differential system into linear and nonlinear subsystems as shown in Fig. 15. The nonlinear subsystem is defined by the map $\widetilde{g} : \widetilde{v} \to \widetilde{i}_\mathrm{g}$. The linear subsystem maps $\widetilde{i}_\mathrm{g}$ to $\widetilde{v}$ through the *linear fractional transformation*, $\mathcal{F} : \mathbb{R}^N \to \mathbb{R}^N$, which is defined as follows:

$$\widetilde{v} = \mathcal{F}(z_\mathrm{osc}I, Y)\widetilde{i}_\mathrm{g} := (I + z_\mathrm{osc}Y)^{-1} z_\mathrm{osc}\widetilde{i}_\mathrm{g}. \qquad (8)$$

Using the small-gain theorem, we can show that the differential system illustrated in Fig. 15 is stable if

$$\widetilde{\gamma}(\mathcal{F}(z_\mathrm{osc}I, Y))\sigma < 1 \qquad (9)$$

where $\widetilde{\gamma} := \sup_{\omega \in \mathbb{R}} \|\mathcal{F}(z_\mathrm{osc}I, Y)\widetilde{i}_\mathrm{g}\|_2 / \|\widetilde{i}_\mathrm{g}\|_2$ is the differential $\mathcal{L}_2$ gain of the linear fractional transformation [39], and $\sigma = |\mathrm{d}g/\mathrm{d}v|$. The $\mathcal{L}_2$ gain of a system provides a measure of the largest amplification imparted to a signal as it propagates through a system. Therefore, (9) implies that as long as the maximum possible amplification around the differential closed-loop system in Fig. 15 is less than unity, then $\widetilde{v}, \widetilde{i}_g \to 0$. Following the approach outlined in [39], and incorporating the current and voltage scaling parameters, ι and ν (see Fig. 3), it can be shown that $\widetilde{\gamma} = \left\| (\iota\nu)^{-1} z_\mathrm{f} z_\mathrm{osc}/((\iota\nu)^{-1} z_\mathrm{f} + z_\mathrm{osc}) \right\|_2$, which establishes the synchronization condition in (1).

Appendix B

Case-Study Parameters

Electrical Network and Inverter-Design Parameters: Oscillator linear-subsystem parameters: $R = 10\,\Omega$, $L = 250\,\mu H$, $C = 28.14$ mF. Oscillator nonlinear-subsystem parameters: $\sigma = 1$ S, $\varphi = 0.47$ V. Inverter voltage gain and nominal current gain: $\nu = 208\sqrt{1/3}$ and $\bar{\iota} = 1.0568 \times 10^{-3}$, respectively. Inverter output filter parameters: $R_f = 0.1\,\Omega$, $L_f = 250\,\mu H$, $C_f = 24\,\mu F$. Dc-bus filter capacitance for Inverter 3: $C_{pv} = 20$ mF. Dc-voltage sources: $v_{dc} = 400$ V. Inverter switching frequency $f_{sw} = 12$ kHz. Line and load parameters (Case studies in Sections IV-A, IV-B, IV-C): $R_{load1} = -,-,25.94\,\Omega$, $R_{load2} = -,-,12.98\,\Omega$, $R_{load3} = 2.60\,\Omega$, $1.16\,\Omega$, $(1.29 \to 1.92 \to 1.29)\,\Omega$, $L_{load3} = -,-,6.90$ mH, $L_{line1} = -,-,2\,\mu H$, $R_{line1} = -,-,2$ mΩ, $L_{line2} = -,-,1\,\mu H$, $R_{line2} = -,-,1$ mΩ.

PV Array and MPPT Controller Parameters: Open-circuit voltage: $V_{oc} = 491$ V, Short-circuit current: $I_{sc} = 41.74$ A, Maximum power point voltage and current: $V_{mpp} = 402$ V, $I_{mpp} = 37.3$ A, respectively. PID-controller parameters: $k_p = 1.057 \times 10^{-4}$ V^{-1}, $k_i = 1.7 \times 10^{-3}$ (V s)$^{-1}$, $k_d = 4.227 \times 10^{-6}$ V^{-1} s, $e_{lim} = 25$ V, $\iota_{min} = -(1/10)\bar{\iota}$, $\iota_{max} = \infty$. EAPO perturbation frequency = 4 Hz, $\rho^{max} = 1.5$, $\rho^{min} = 0.5$, $\xi = 0.0167$.

References

[1] H. Khalil, *Nonlinear Systems*, 3rd ed. Upper Saddle River, NJ, USA: Prentice–Hall, 2002.

[2] L. A. B. Tôrres, J. P. Hespanha, and J. Moehlis, "Power supplies synchronization without communication," in *Proc. Power Energy Soc. General Meet.*, Jul. 2012, pp. 1–6.

[3] B. B. Johnson, S. V. Dhople, A. O. Hamadeh, and P. T. Krein, "Synchronization of nonlinear oscillators in an LTI power network," *IEEE Trans. Circuits Syst. I, Fundam. Theory Appl.*, to be published.

[4] B. Johnson, S. Dhople, A. Hamadeh, and P. Krein, "Synchronization of parallel single-phase inverters using virtual oscillator control," *IEEE Trans. Power Electron.*, submitted for publication.

[5] M. Chandorkar, D. Divan, and R. Adapa, "Control of parallel connected inverters in standalone AC supply systems," *IEEE Trans. Ind. Appl.*, vol. 29, no. 1, pp. 136–143, Jan. 1993.

[6] J. Lopes, C. Moreira, and A. Madureira, "Defining control strategies for microgrids islanded operation," *IEEE Trans. Power Syst.*, vol. 21, no. 2, pp. 916–924, May 2006.

[7] R. Lasseter, "Microgrids," in *Proc. IEEE Power Eng. Soc. Winter Meet.*, 2002, vol. 1, pp. 305–308.

[8] P. Piagi and R. Lasseter, "Autonomous control of microgrids," in *Proc. IEEE Power Eng. Soc. General Meet.*, Jun. 2006, vol. 6, pp. 1–8.

[9] J. M. Guerrero, J. Matas, L. G. de Vicuña, M. Castilla, and J. Miret, "Wireless-control strategy for parallel operation of distributed-generation inverters," *IEEE Trans. Ind. Electron.*, vol. 53, no. 5, pp. 1461–1470, Oct. 2006.

[10] J. M. Guerrero, J. C. Vasquez, J. Matas, M. Castilla, and L. G. de Vicuna, "Control strategy for flexible microgrid based on parallel line-interactive UPS systems," *IEEE Trans. Ind. Electron.*, vol. 56, no. 3, pp. 726–736, Mar. 2009.

[11] J. Vasquez, J. Guerrero, M. Savaghebi, J. Eloy-Garcia, and R. Teodorescu, "Modeling, analysis, and design of stationary-reference-frame droop-controlled parallel three-phase voltage source inverters," *IEEE Trans. Ind. Electron.*, vol. 60, no. 4, pp. 1271–1280, Apr. 2013.

[12] J. Guerrero, L. de Vicuna, J. Matas, M. Castilla, and J. Miret, "A wireless controller to enhance dynamic performance of parallel inverters in distributed generation systems," *IEEE Trans. Power Electron.*, vol. 19, no. 5, pp. 1205–1213, Sep. 2004.

[13] F. Katiraei and M. Iravani, "Power management strategies for a microgrid with multiple distributed generation units," *IEEE Trans. Power Syst.*, vol. 21, no. 4, pp. 1821–1831, Nov. 2006.

[14] A. Mohd, D. Ortjohann, and O. Omari, "Review of control techniques for inverters parallel operation," *Electr. Power Syst. Res.*, vol. 80, pp. 1477–1487, Dec. 2010.

[15] M. Marwali, J.-W. Jung, and A. Keyhani, "Control of distributed generation systems—Part II: Load sharing control," *IEEE Trans. Power Electron.*, vol. 19, no. 6, pp. 1551–1561, Nov. 2004.

[16] J. M. Guerrero, J. C. Vasquez, J. Matas, L. G. de Vicuña, and M. Castilla, "Hierarchical control of droop-controlled AC and DC microgrids—A general approach toward standardization," *IEEE Trans. Ind. Electron.*, vol. 58, no. 1, pp. 158–172, Jan. 2011.

[17] J. He and Y. W. Li, "An enhanced microgrid load demand sharing strategy," *IEEE Trans. Power Electron.*, vol. 27, no. 9, pp. 3984–3995, Sep. 2012.

[18] Q.-C. Zhong, "Robust droop controller for accurate proportional load sharing among inverters operated in parallel," *IEEE Trans. Ind. Electron.*, vol. 60, no. 4, pp. 1281–1290, Apr. 2013.

[19] J. M. Guerrero, M. Chandorkar, T. Lee, and P. C. Loh, "Advanced control architectures for intelligent microgrids—Part I: Decentralized and hierarchical control," *IEEE Trans. Ind. Electron.*, vol. 60, no. 4, pp. 1254–1262, Apr. 2013.

[20] A. Mauroy, P. Sacré, and R. J. Sepulchre, "Kick synchronization versus diffusive synchronization," in *Proc. IEEE Conf. Decis. Control*, 2012, pp. 7171–7183.

[21] A. Yazdani and R. Iravani, *Voltage-Sourced Converters in Power Systems*. Hoboken, NJ, USA: Wiley, 2010.

[22] D. Holmes and T. Lipo, *Pulse Width Modulation for Power Converters*. Piscataway, NJ, USA: IEEE Press, 2003.

[23] S. Golestan, M. Joorabian, H. Rastegar, A. Roshan, and J. Guerrero, "Droop based control of parallel-connected single-phase inverters in D-Q rotating frame," in *Proc. IEEE Int. Conf. Ind. Tech.*, 2009, pp. 1–6.

[24] U. A. Miranda, L. G. B. Rolim, and M. Aredes, "A DQ synchronous reference frame current control for single-phase converters," in *Proc. IEEE Power Electron. Spec. Conf.*, 2005, pp. 1377–1381.

[25] V. T. Buyukdegirmenci, A. M. Bazzi, and P. T. Krein, "A comparative study of an exponential adaptive perturb and observe algorithm and ripple correlation control for real-time optimization," in *Proc. IEEE Workshop Control Model. Power Electron.*, 2010, pp. 1–8.

[26] W. Xiao and W. G. Dunford, "A modified adaptive hill climbing MPPT method for photovoltaic power systems," in *Proc. IEEE Power Electron. Spec. Conf.*, 2004, vol. 3, pp. 1957–1963.

[27] N. Fermia, D. Granozio, G. Petrone, and M. Vitelli, "Predictive adaptive MPPT perturb and observe method," *IEEE Trans. Aerosp. Electron. Syst.*, vol. 43, no. 3, pp. 934–950, Jul. 2007.

[28] C. Zhang and D. Zhao, "A novel MPPT method with variable perturbation step for photovoltaic system," in *Proc. IEEE Conf. Ind. Electron. Appl.*, 2009, pp. 2184–2187.

[29] K. A. Kim, P. T. Krein, J. J. Lee, H. Bae, and B.-H. Cho, "Irradiance and temperature transient sensitivity analysis for photovoltaic control," in *Proc. IEEE Int. Conf. Power Electron. Energy Convers. Congr. Expo Asia*, 2011, pp. 393–400.

[30] T. Esram and P. L. Chapman, "Comparison of photovoltaic array maximum power point tracking techniques," *IEEE Trans. Energy Convers.*, vol. 22, no. 2, pp. 439–449, Jun. 2007.

[31] A. Bidram, A. Davoudi, and R. S. Balog, "Control and circuit techniques to mitigate partial shading effects in photovoltaic arrays," *IEEE J. Photovolt.*, vol. 2, no. 4, pp. 532–546, Oct. 2012.

[32] M. de Brito, L. Galotto, L. Sampaio, G. de Azevedo e Melo, and G. Canesin, "Evaluation of the main MPPT techniques for photovoltaic applications," *IEEE Trans. Ind. Electron.*, vol. 60, no. 3, pp. 1156–1167, Mar. 2013.

[33] D. Sera, L. Mathe, T. Kerekes, S. Spataru, and R. Teodorescu, "On the perturb-and-observe and incremental conductance MPPT methods for PV systems," *IEEE J. Photovolt.*, vol. 3, no. 3, pp. 1070–1078, Jul. 2013.

[34] P. E. Kakosimos, A. G. Kladas, and S. N. Manias, "Fast photovoltaic-system voltage- or current-oriented MPPT employing a predictive digital current-controlled converter," *IEEE Trans. Ind. Electron.*, vol. 60, no. 12, pp. 5673–5685, Dec. 2013.

[35] B. N. Alajmi, K. H. Ahmed, S. J. Finney, and B. W. Williams, "A maximum power point tracking technique for partially shaded photovoltaic systems in microgrids," *IEEE Trans. Ind. Electron.*, vol. 60, no. 4, pp. 1596–1606, Apr. 2013.

[36] G.-C. Hsieh, H.-I. Hsieh, C.-Y. Tsai, and C.-H. Wang, "Photovoltaic power-increment-aided incremental-conductance MPPT with two-phased

tracking," *IEEE Trans. Power Electron.*, vol. 28, no. 6, pp. 2895–2911, Jun. 2013.

[37] E. Dallago, D. G. Finarelli, U. P. Gianazza, A. L. Barnabei, and A. Liberale, "Theoretical and experimental analysis of an MPP detection algorithm employing a single-voltage sensor only and a noisy signal," *IEEE Trans. Power Electron.*, vol. 28, no. 11, pp. 5088–5097, Nov. 2013.

[38] G. M. Masters, *Renewable and Efficient Electric Power Systems*. Hoboken, NJ, USA: Wiley-Interscience, 2004.

[39] A. Hamadeh, "Constructive robust synchronization of networked control systems," Ph.D. dissertation, Dept. Eng., Univ. Cambridge, U.K., Jun. 2010.

Abdullah O. Hamadeh received the M.Eng., M.A., and Ph.D. degrees in electrical engineering from the University of Cambridge, Cambridge, U.K., in 2005, 2008, and 2010 respectively. His doctoral research concerned the control and synchronization of networked dynamical systems.

Between 2010 and 2013, he held Postdoctoral positions with the University of Waterloo, Waterloo, ON, Canada, and Rutgers University, New Brunswick, NJ, USA. He is currently a Post-Doctoral Associate with the Department of Mechanical Engineering, Massachusetts Institute of Technology, Cambridge, MA, USA. His current research interests are in the applications of control theoretic techniques to systems and synthetic biology and in the control of electrical power networks.

Brian B. Johnson (S'08–M'13) received the B.S. degree in physics from Texas State University, San Marcos, TX, USA, in 2008 and the M.S. and Ph.D. degrees in electrical and computer engineering from the University of Illinois at Urbana-Champaign, Urbana, IL, USA, in 2010 and 2013, respectively.

He is currently an Electrical Engineer with the National Renewable Energy Laboratory, Golden, CO, USA. His research interests include power electronics, distributed generation, renewable energy systems, and nonlinear controls.

Dr. Johnson received a National Science Foundation Graduate Research Fellowship in 2010.

Philip T. Krein (S'76–M'82–SM'93–F'00) received the B.S. degree in electrical engineering and the A.B. degree in economics and business from Lafayette College, Easton, PA, USA, and the M.S. and Ph.D. degrees in electrical engineering from the University of Illinois (UI), Urbana, IL, USA.

He was an Engineer with Tektronix, Beaverton, OR, USA, and then returned to UI. He currently holds the Grainger Endowed Director's Chair with Electric Machinery and Electromechanics as a Professor and the Director of the Department of Electrical and Computer Engineering, Grainger Center for Electric Machinery and Electromechanics, UI. He has published an undergraduate textbook *Elements of Power Electronics* (Oxford, U.K.: Oxford Univ. Press, 1998). In 2001, he helped initiate the IEEE International Future Energy Challenge: a major student competition involving fuel cell power conversion and energy efficiency. He holds 26 U.S. patents with additional patents pending. His research interests include all the aspects of power electronics, machines, drives, and electrical energy, with emphasis on nonlinear control and distributed systems.

Dr. Krein is a Registered Professional Engineer in Illinois and Oregon. He was a senior Fulbright Scholar with the University of Surrey, Surrey, U.K., and was recognized as a University Scholar, which is the highest research award at UI. In 2003, he received the IEEE William E. Newell Award in Power Electronics. He is a past President of the IEEE Power Electronics Society and served as a member of the IEEE Board of Directors. During 2005–2007, he was a Distinguished Lecturer for the IEEE Power Electronics Society. In 2008, he received the Distinguished Service Award from the IEEE Power Electronics Society. He is an Associate Editor of the IEEE TRANSACTIONS ON POWER ELECTRONICS and serves as an Academic Advisor for the Department of Electronic and Information Engineering, Hong Kong Polytechnic University. He is a Founder and the Director of SolarBridge Technologies: a developer of long-life integrated solar energy systems.

Sairaj V. Dhople (S'09–M'13) received the B.S., M.S., and Ph.D. degrees in electrical engineering, in 2007, 2009, and 2012, respectively, from the University of Illinois, Urbana-Champaign, Urbana, IL, USA.

He is currently an Assistant Professor with the Department of Electrical and Computer Engineering, University of Minnesota, Minneapolis, MN, USA, where he is affiliated with the Power and Energy Systems research group. His research interests include modeling, analysis, and control of power electronics and power systems with a focus on renewable integration.

James L. Cale (M'03) received the B.S. (summa cum laude) degree in electrical engineering from the University of Missouri-Rolla, Rolla, MO, USA, in 2001 and the M.S. and Ph.D. degrees in electrical engineering from Purdue University, West Lafayette, IN, USA, in 2003 and 2007, respectively.

His background and research interests include areas of high-penetration photovoltaic (PV) integration on the electric grid, power electronic controls, and microgrids. Prior to joining The National Renewable Energy Laboratory (NREL), Golden, CO, USA, he was a Member of Technical Staff with Advanced Energy, where he designed controls for advanced utility-scale PV inverters. He currently manages the Distributed Energy Systems Integration group, NREL.